Rational Design, Synthesis, Evaluation, and Crystal Structure of a Potent Inhibitor of Human GAR Tfase: 10-(Trifluoroacetyl)-5,10-dideazaacyclic-5,6,7,8-tetrahydrofolic Acid[†,‡]

Yan Zhang,[§,||] Joel Desharnais,[⊥] Thomas H. Marsilje,[⊥] Chenglong Li,[§] Michael P. Hedrick,[⊥] Lata T. Gooljarsingh,[@] Ali Tavassoli,[@] Stephen J. Benkovic,[@] Arthur J. Olson,[§] Dale L. Boger,*[,||,⊥] and Ian A. Wilson*[,§,||]

Departments of Molecular Biology and Chemistry and The Skaggs Institute for Chemical Biology, The Scripps Research Institute, 10550 North Torrey Pines Road, La Jolla, California 92037, and Department of Chemistry, Pennsylvania State University, University Park, Pennsylvania 16802

Received February 6, 2003; Revised Manuscript Received April 8, 2003

ABSTRACT: Glycinamide ribonucleotide transformylase (GAR Tfase) has been the target of anti-neoplastic intervention for almost two decades. Here, we use a structure-based approach to design a novel folate analogue, 10-(trifluoroacetyl)-5,10-dideazaacyclic-5,6,7,8-tetrahydrofolic acid (10-CF_3CO-DDACTHF, **1**), which specifically inhibits recombinant human GAR Tfase (K_i = 15 nM), but is inactive (K_i > 100 μM) against other folate-dependent enzymes that have been examined. Moreover, compound **1** is a potent inhibitor of tumor cell proliferation (IC_{50} = 16 nM, CCRF-CEM), which represents a 10-fold improvement over Lometrexol, a GAR Tfase inhibitor that has been in clinical trials. Thus, this folate analogue **1** is among the most potent and selective inhibitors known toward GAR Tfase. Contributing to its efficacious activity, compound **1** is effectively transported into the cell by the reduced folate carrier and intracellularly sequestered by polyglutamation. The crystal structure of human GAR Tfase with folate analogue **1** at 1.98 Å resolution represents the first structure of any GAR Tfase to be determined with a cofactor or cofactor analogue without the presence of substrate. The folate-binding loop of residues 141−146, which is highly flexible in both *Escherichia coli* and unliganded human GAR Tfase structures, becomes highly ordered upon binding **1** in the folate-binding site. Computational docking of the natural cofactor into this and other apo or complexed structures provides a rational basis for modeling how the natural cofactor 10-formyltetrahydrofolic acid interacts with GAR Tfase, and suggests that this folate analogue-bound conformation represents the best template to date for inhibitor design.

Glycinamide ribonucleotide transformylase (GAR Tfase)[1] is a folate-dependent enzyme within the *de novo* purine biosynthetic pathway (*1*−*3*; review in ref *4*). GAR Tfase utilizes the cofactor 10-formyltetrahydrofolic acid (10-formyl-THF) in the third step of the pathway to transfer a formyl group to the primary amine of its substrate, β-glycinamide ribonucleotide (β-GAR). GAR Tfase is of mechanistic interest for the ease with which it catalyzes the formyl transfer (*5*, *6*), of biological interest for its role in the synthesis of DNA precursor purines (*7*), of structural interest for delineation of key mechanistic features of its catalytic reaction (*8*−*11*), and of medicinal interest as an important target for chemotherapeutic drug design (*12*−*17*).

Inhibitors of folate metabolism have provided important agents for cancer chemotherapy as a result of their inhibition of the biosynthesis of nucleic acid precursors (reviewed in refs *18* and *19*). Validation of GAR Tfase as an anticancer target came in the 1980s with the discovery of the first potent and selective inhibitor, 5,10-dideaza-5,6,7,8-tetrahydrofolic acid (DDATHF) (*12*). This compound exhibits effective activity *in vivo* against solid murine and human tumors, where Methotrexate (MTX) has little effect. The selectivity of DDATHF has been attributed to the reliance of tumor cells on *de novo* purine synthesis, while the salvage pathway is the primary source of purines in most normal cells. The 6*R* diastereomer, Lometrexol (LTX, K_i = 60 nM) (Figure 1), has been in and out of clinical trials, initially as a

[†] This work was supported by National Institutes of Health Grants PO1 CA63536 (I.A.W., D.L.B., and S.J.B.) and P41 RR08605 (A.J.O.), National Cancer Institute Grant R24 CA95830 (A.J.O.), and a Skaggs predoctoral fellowship (Y.Z.).

[‡] This is publication 15499-CH from The Scripps Research Institute.

* To whom correspondence should be addressed. I.A.W.: e-mail, wilson@scripps.edu; phone, (858) 784-9706; fax, (858) 784-2980. D.L.B.: e-mail, boger@scripps.edu; phone, (858) 784-7522; fax, (858) 784-7550.

[§] Department of Molecular Biology, The Scripps Research Institute.

[⊥] Department of Chemistry, The Scripps Research Institute.

[||] The Skaggs Institute for Chemical Biology, The Scripps Research Institute.

[@] Pennsylvania State University.

[1] Abbreviations: GAR Tfase, glycinamide ribonucleotide transformylase; 10-CF_3CO-DDACTHF, 10-(trifluoroacetyl)-5,10-dideazaacyclic-5,6,7,8-tetrahydrofolic acid; AICAR Tfase, 5-aminoimidazole-4-carboxamide-ribonucleotide transformylase; 10-formyl-THF, 10-formyltetrahydrofolic acid; β-GAR, β-glycinamide ribonucleotide; DHFR, dihydrofolate reductase; DDATHF, 5,10-dideaza-5,6,7,8-tetrahydrofolic acid; FPGS, folylpolyglutamate synthetase; 10-formyl-TDAF, 10-formyl-5,8,10-trideazafolic acid; 10-formyl-DDACTHF, 10-formyl-5,10-dideazaacyclic-5,6,7,8-tetrahydrofolic acid; TS, thymidylate synthetase; fDDF, 10-formyl-5,8-dideazafolic acid; DMSO, dimethyl sulfoxide; SSRL, Stanford Synchrotron Radiation Laboratory; rmsd, root-mean-square deviation; MR, molecular replacement.

10.1021/bi034219c CCC: $25.00 © 2003 American Chemical Society
Published on Web 05/06/2003

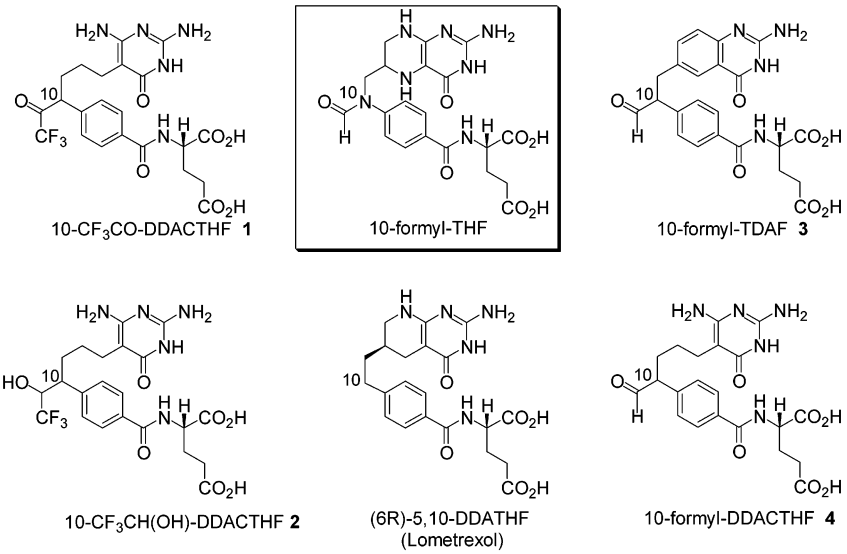

FIGURE 1: Natural cofactor 10-formyl-THF and representative folate analogue inhibitors of GAR Tfase.

consequence of its effective anti-neoplastic activity (*20*) and, more recently, due to the reduction of its general toxicity when supplemented with folic acid (*21*, *22*).

Human GAR Tfase (purN) is located at the C-terminus of a trifunctional enzyme encoded by purD-purM-purN with a molecular mass of more than 110 kDa. The other two enzyme activities are GAR synthetase (purD) and AIR synthetase (purM), which represent steps 2 and 5 in the *de novo* purine biosynthetic pathway (*23*−*25*). Because of the complexity of the trifunctional enzyme, the majority of the biological and structural studies of GAR Tfase have been performed with the protein isolated from bacterial sources; the sequence of the *Escherichia coli* enzyme is overall 31% identical with its human counterpart, but that increases to almost 100% within the active site. The monofunctional *E. coli* GAR Tfase with a molecular mass of 23 kDa has been a useful surrogate target for the human enzyme for mechanistic studies for many years (*6*, *26*, *27*), and more recently for inhibitor design (*16*, *28*−*30*). However, an understanding of any subtleties in the activity and function of human versus bacterial GAR Tfase function has been hampered by the lack of any structural data for mammalian GAR Tfases. For example, the mammalian polyglutamation of the folate cofactor entails only γ-carboxylate linkages in the glutamate tail (*31*−*33*), whereas α and γ polyglutamation are observed in *E. coli* and other bacterial systems (*34*, *35*); presumably, the human and *E. coli* GAR Tfase structures may reflect such differences in their interaction with the polyglutamated tail.

Our recently determined structure of recombinant human GAR Tfase (rhGAR Tfase) revealed a number of important differences between the human and *E. coli* enzymes (*11*). Recombinant human GAR Tfase exists as a monomer at a wide range of pH values, in contrast to the dimerization observed for *E. coli* GAR Tfase below pH 6.8. The active site loop helix (residues 110−131) that undergoes a pH-dependent order−disorder transition in *E. coli* GAR Tfase has a uniform conformation under all pH ranges that were tested (pH 4−9) in the human enzyme. Although the substrate-binding pocket in *E. coli* GAR Tfase always adopts the same conformation under a wide range of pH conditions (pH 3.5−8), a loop (residues 8−14) in the human enzyme changes from an open to an occluded conformation at low pH that appears to prohibit the substrate binding. Most importantly, the folate-binding loop, which intimately interacts with bound folate analogues, adopts conformations in the unliganded human GAR Tfase different from those described previously for the *E. coli* enzyme.

Here, we have utilized the knowledge obtained from various X-ray structures of GAR Tfase to design a novel compound that acts as a tight binding, specific inhibitor of GAR Tfase. A previous structure of *E. coli* GAR Tfase (PDB entry 1C2T) in complex with substrate and 10-formyl-TDAF (**3**, Figure 1), a cofactor analogue bearing a nontransferable formyl group (*E. coli* GAR Tfase K_i = 260 nM), revealed that the inhibitor bound as the hydrated aldehyde (gem-diol) in the enzyme active site (*10*), mimicking the formyl transfer tetrahedral intermediate.

As a result of the synthesis and evaluation of an extensive series of related candidate inhibitors, mainly based on the *E. coli* GAR Tfase complex structures, we report the design, synthesis, and evaluation of a novel folate analogue, 10-CF_3CO-DDACTHF (**1**) (Figure 1). This compound exhibits selective and tight binding affinity toward human GAR Tfase (K_i = 15 nM) and is at least 10 times more potent than Lometrexol in cytotoxic assays. The analogue also exhibits excellent stability and solubility at pH 7−8, and possesses a number of additional properties that make it an excellent candidate for *in vivo* antitumor testing in animal models. The crystal structure of human GAR Tfase with the inhibitor at 1.98 Å resolution at physiological pH defines the detailed interactions and geometry of the inhibitor within the active site, and provides the best model to date for computational docking studies for exploring the mechanism of binding of the natural folate cofactor. Docking of 10-formyl-THF (Figure 1) into the binding site strongly supports the conclusions from the kinetic and mutagenesis data for the central role played by the catalytic triad (His108, Asp144, and Asn106), and provides a more physiologically relevant model on which to base future inhibitor designs.

MATERIALS AND METHODS

Materials

Luria broth and agar were obtained from Life Technologies (Gaithersburg, MD). All common buffers and reagents were purchased from Sigma-Aldrich Corp. (St. Louis, MO).

*Synthesis and Characterization of 10-CF_3CO-DDACTHF (**1**)*

*Methyl 4-(3,3,3-Trifluoro-2-oxopropyl)benzoate (**6**).* Known acid chloride **5** (37.7 g, 177 mmol) was dissolved in anhydrous CH_2Cl_2 (500 mL) and cooled to −60 °C. Trifluoroacetic anhydride (77.0 mL, 543 mmol, 3 equiv) was added slowly to the stirring solution. Anhydrous pyridine (30.0 mL, 371 mmol, 2 equiv) was added dropwise, and the reaction mixture was stirred at −60 °C for 4 h. The reaction was quenched by the dropwise addition of H_2O (35 mL) to the stirring solution, followed by warming to 25 °C. The reaction mixture was partitioned between H_2O (600 mL) and CH_2Cl_2 (100 mL). The organic layer was washed with 1 N HCl (2 × 500 mL) and saturated aqueous NaCl (500 mL) followed by concentration under reduced pressure. Chromatography (SiO_2, 1:1 hexanes/EtOAc) afforded **6** (41.3 g, 95%) as a yellow oil: ^{1}H NMR (CD_3OD, 400 MHz) δ 7.90 (d, J = 8.5 Hz, 2H), 7.39 (d, J = 8.2 Hz, 2H), 3.87 (s, 3H), 3.10 (s, 2H); ^{13}C NMR (CD_3OD, 100 MHz) δ 168.8, 141.7, 132.3, 131.5, 130.8, 130.1, 129.9, 52.7, 41.2; MALDIFTMS (DHB) m/z 245.0436 ($M - H^+$, $C_{11}H_9F_3O_3$ requires 245.0431).

*Methyl 4-(3,3,3-Trifluoro-2-dimethylhydrazonopropyl)benzoate (**7**).* Compound **6** (35.6 g, 145 mmol) was dissolved in anhydrous EtOH (600 mL). *N*,*N*-Dimethylhydrazine (55.0 mL, 724 mmol, 5 equiv) was added to this solution followed by glacial acetic acid (8.30 mL, 145 mmol, 1 equiv), and the mixture was stirred at 25 °C for 48 h. The reaction mixture was concentrated under reduced pressure. Chromatography (SiO_2, 2:1 hexanes/EtOAc) afforded **7** (26.8 g, 64%) as a yellow oil: ^{1}H NMR ($CDCl_3$, 250 MHz) δ 7.97 (d, J = 8.0 Hz, 2H), 7.23 (d, J = 8.8 Hz, 2H), 3.92 (s, 2H), 3.89 (s, 3H), 2.79 (s, 6H); MALDIFTMS (DHB) m/z 289.1166 ($M + H^+$, $C_{13}H_{15}F_3N_2O_2$ requires 289.1158).

*Methyl 4-[4-Bromo-1-(2,2,2-trifluoro-1-dimethylhydrazonoethyl)butyl]benzoate (**8**).* NaH (60% dispersion, 2.34 g, 58.6 mmol, 1 equiv) was added to a stirred solution of **7** (16.7 g, 58.1 mmol) in anhydrous DMF (250 mL) at 0 °C. The solution was stirred at 0 °C for 15 min. 1,3-Dibromopropane (35.0 mL, 345 mmol, 6 equiv) was added quickly to the reaction mixture, and the cooling bath was removed. The reaction mixture was stirred at 25 °C for 2.5 h. The reaction was quenched by the addition of saturated aqueous NH_4Cl (150 mL). The reaction mixture was partitioned between EtOAc (600 mL) and H_2O (400 mL). The organic layer was washed with H_2O (2 × 500 mL) and saturated aqueous NaCl (1 × 500 mL) followed by concentration under reduced pressure. Chromatography (SiO_2, 4:1 hexanes/EtOAc) afforded **8** (15.4 g, 65%) as a yellow oil: ^{1}H NMR ($CDCl_3$, 250 MHz) δ 7.98 (d, J = 8.4 Hz, 2H), 7.36 (d, J = 8.0 Hz, 2H), 4.77 (t, J = 7.7 Hz, 0.5H), 4.18−4.04 (m, 0.5H), 3.89 (s, 3H), 3.45 (t, J = 6.4 Hz, 1H), 3.39−3.30 (m, 1H), 2.78 (s, 2H), 2.60 (s, 4H), 2.41−2.28 (m, 1H), 2.21−2.02 (m, 1H), 2.00−1.75 (m, 2H); MALDIFTMS (DHB) m/z 409.0723 ($M + H^+$, $C_{16}H_{20}BrF_3N_2O_2$ requires 409.0733).

*Methyl 4-[4-Cyano-4-ethoxycarbonyl-1-(2,2,2-trifluoro-1-dimethylhydrazonoethyl)butyl]benzoate (**9**).* A suspension of NaH (60% dispersion, 26.0 g, 655 mmol, 18 equiv) in anhydrous DMF (300 mL) at 0 °C was treated dropwise with ethyl cyanoacetate (70.0 mL, 657 mmol, 18 equiv). The reaction mixture was stirred at 0 °C for 30 min, forming the sodium salt as a clear solution. This anion was treated with a solution of **8** (14.4 g, 35.7 mmol) in anhydrous DMF (300 mL). The reaction mixture was stirred at 25 °C for 2 h before the reaction was quenched by the addition of saturated aqueous NH_4Cl (50 mL). The reaction mixture was diluted with EtOAc (600 mL) and washed with H_2O (5 × 400 mL) and saturated aqueous NaCl (400 mL). The organic layer was dried (Na_2SO_4), filtered, and concentrated under reduced pressure. The excess ethyl cyanoacetate was distilled off, and the residual product was purified by chromatography (SiO_2, 7:1 hexanes/EtOAc), affording **9** (11.2 g, 71%) as a yellow oil: ^{1}H NMR ($CDCl_3$, 400 MHz) δ 8.06 (d, J = 8.4 Hz, 2H), 7.42 (d, J = 8.4 Hz, 2H), 4.85 (t, J = 7.7 Hz, 1H), 4.32 (q, J = 7.7 Hz, 2H), 3.97 (s, 3H), 3.57 (m, 1H), 2.85 (s, 2H), 2.68 (s, 4H), 2.30 (m, 1H), 2.11 (m, 3H), 1.90−1.63 (m, 2H), 1.36 (t, J = 7.7 Hz, 3H); MALDIFTMS (DHB) m/z 464.1768 ($M + Na^+$, $C_{21}H_{26}F_3N_3O_4Na$ requires 409.1768).

*Methyl 4-[4-(2,4-Diamino-6-oxo-1,6-dihydropyrimidin-5-yl)-1-(2,2,2-trifluoro-1-dimethylhydrazonoethyl)butyl]-benzoate (**10**).* Sodium metal (0.71 g, 30.9 mmol, 2 equiv) was added to anhydrous CH_3OH (15 mL), and the reaction mixture was stirred at 25 °C for 10 min to generate $NaOCH_3$. Guanidine-HCl (1.47 g, 15.4 mmol, 1 equiv) was added, and the reaction mixture was stirred at 25 °C for 30 min. Separately, **9** (6.78 g, 15.4 mmol) was dissolved in anhydrous CH_3OH (15 mL), and this solution was added quickly to the stirring reaction mixture. The resulting reaction mixture was stirred at reflux for 16 h. The reaction mixture was applied directly to a SiO_2 plug. Impurities were removed by washing with a 3:1 hexanes/EtOAc mixture. The product was subsequently eluted by washing with a 10:1 $CHCl_3/CH_3OH$ mixture to afford **10** (3.91 g, 56%) as a tan solid: ^{1}H NMR (CD_3OD, 250 MHz) δ 7.94 (d, J = 8.4 Hz, 2H), 7.41 (d, J = 8.4 Hz, 2H), 4.78 (t, J = 7.7 Hz, 1H), 3.88 (s, 3H), 2.82 (s, 1H), 2.61 (s, 5H), 2.40 (t, J = 6.4 Hz, 2H), 2.39−2.22 (m, 1H), 2.10−1.91 (m, 1H), 1.65−1.42 (m, 2H); MALDIFTMS (DHB) m/z 455.2001 ($M + H^+$, $C_{20}H_{25}F_3N_6O_3$ requires 455.2013).

*4-[4-(2,4-Diamino-6-oxo-1,6-dihydropyrimidin-5-yl)-1-(2,2,2-trifluoroacetyl)butyl]benzoic Acid (**11**).* A solution of **10** (2.11 g, 4.64 mmol) in a 3:1 CH_3OH/H_2O mixture (80 mL) was treated with a $LiOH/1H_2O$ mixture (0.59 g, 13.9 mmol, 3 equiv), and the reaction mixture was stirred at 25 °C for 24 h. The reaction mixture was diluted with H_2O (100 mL), and the aqueous layer was washed with EtOAc (100 mL). The aqueous layer was acidified to pH 4 by the addition of 1 N aqueous HCl. The reaction mixture was concentrated under reduced pressure, and the residue was treated with MeCN (3 × 100 mL) to remove traces of H_2O to provide **11** (1.84 g, 100%) which was used without further purification: ^{1}H NMR (CD_3OD, 250 MHz) δ 8.00 (d, J = 8.1 Hz, 1H), 7.89 (d, J = 8.4 Hz, 1H), 7.40 (d, J = 8.1 Hz, 1H), 7.37 (d, J = 8.1 Hz, 1H), 4.37 (t, J = 7.2 Hz, 0.3H), 3.15−3.00 (m, 0.7H), 2.33 (t, J = 7.4 Hz, 1H), 2.25 (t, J = 7.4 Hz, 1H), 2.19−1.77 (m, 2H), 1.44−1.25 (m, 2H);

MALDIFTMS (DHB) *m/z* 399.1275 ($M + H^+$, $C_{17}H_{17}F_3N_4O_4$ requires 399.1275).

*Di-tert-butyl N-{4-[4-(2,4-Diamino-6-oxo-1,6-dihydropyrimidin-5-yl)-1-(2,2,2-trifluoroacetyl)butyl]benzoyl}-L-glutamate (**12**).* A solution of **11** (1.84 g, 4.62 mmol) and di-*tert*-butyl L-glutamate hydrochloride (1.71 g, 4.76 mmol, 1 equiv) in DMF (20 mL) was treated with $NaHCO_3$ (1.41 g, 16.8 mmol, 4 equiv) followed by EDCI (1.71 g, 8.9 mmol, 2 equiv). The reaction mixture was stirred at 25 °C for 48 h before the solvent was removed under reduced pressure. The resulting residue was suspended in $CHCl_3$ (300 mL) and washed with saturated aqueous $NaHCO_3$ (2 × 300 mL). The organic layer was dried (Na_2SO_4), filtered, and concentrated under reduced pressure. Chromatography (SiO_2, 10:1 $CHCl_3$/CH_3OH) afforded **12** (1.29 g, 44%) as a yellow solid: ^{1}H NMR (CD_3OD, 250 MHz) δ 7.71 (d, J = 8.4 Hz, 2H), 7.40 (d, J = 8.4 Hz, 2H), 4.52−4.45 (m, 1H), 3.17−3.00 (m, 1H), 2.42−2.10 (m, 3H), 2.39 (t, J = 6.9 Hz, 2H), 2.09−1.97 (m, 2H), 1.92−1.78 (m, 1H), 1.50−1.38 (m, 2H), 1.48 (s, 9H), 1.42 (s, 9H); MALDIFTMS (DHB) *m/z* 640.2975 ($M + H^+$, $C_{30}H_{40}F_3N_5O_7$ requires 640.2952).

*N-{4-[4-(2,4-Diamino-6-oxo-1,6-dihydropyrimidin-5-yl)-1-(2,2,2-trifluoroacetyl)butyl]benzoyl}-L-glutamic Acid (**1**).* A solution of **12** (1.29 g, 2.02 mmol) in $CHCl_3$ (120 mL) cooled to 0 °C was treated with trifluoroacetic acid (35 mL). The reaction mixture was allowed to warm and stirred at 25 °C for 12 h. The reaction mixture was concentrated under reduced pressure. Et_2O (75 mL) was added, and a precipitate formed. The precipitate was collected, triturated with Et_2O (3 × 75 mL), and dried *in vacuo* to give **1**-CF_3CO_2H (1.30 g, 100%) as a white solid: ^{1}H NMR (CD_3OD, 400 MHz) δ 7.84 (d, J = 7.9 Hz, 0.6H), 7.73 (d, J = 8.2 Hz, 1.3H), 7.39 (d, J = 8.5 Hz, 1.3H), 7.36 (d, J = 8.2 Hz, 0.6H), 4.65−4.60 (m, 1H), 3.12−3.02 (m, 0.4H), 2.48 (t, J = 6.8 Hz, 2H), 2.42−2.20 (m, 2H), 2.30 (t, J = 7.2 Hz, 1.4H), 2.23 (t, J = 7.3 Hz, 0.6H), 2.12−1.94 (m, 3H), 1.91−1.73 (m, 1H); MALDIFTMS (DHB) *m/z* 528.1709 ($M + H^+$, $C_{22}H_{24}F_3N_5O_7$ requires 528.1701).

*N-{4-[4-(2,4-Diamino-6-oxo-1,6-dihydropyrimidin-5-yl)-1-(2,2,2-trifluoro-1-hydroxyethyl)butyl]benzoyl}-L-glutamic Acid (**2**).* A solution of **12** (0.010 g, 0.016 mmol) in anhydrous CH_3OH (0.5 mL) at −20 °C was treated with $NaBH_4$ (0.0012 g, 0.031 mmol, 2.0 equiv). The reaction mixture was stirred at −20 °C for 30 min before the reaction was quenched by the addition of H_2O (1 mL). The mixture was diluted with EtOAc (5 mL) and washed with H_2O (2 × 1 mL). The organic layer was dried (Na_2SO_4), filtered, and concentrated under reduced pressure. The resulting product (0.009 g, 0.014 mmol) was treated with 4 N HCl-dioxane (2 mL) at 0 °C, and the solution was allowed to warm and stir at 25 °C for 3 h. The reaction mixture was purged with N_2 and then concentrated under reduced pressure. Et_2O (1 mL) was added, and a precipitate formed. The precipitate was collected, triturated with Et_2O (3 × 1 mL), and dried *in vacuo* to give **2**-HCl (0.004 g, 90% from **1**) as a yellow solid: ^{1}H NMR (CD_3OD, 400 MHz) δ 7.75 (d, J = 8.2 Hz, 2H), 7.39 (d, J = 8.2 Hz, 2H), 4.65−4.58 (m, 1H), 4.22−4.12 (m, 1H), 3.06−3.00 (m, 1H), 2.57−2.42 (m, 1H), 2.48 (t, J = 7.5 Hz, 2H), 2.40−2.22 (m, 2H), 2.29 (t, J = 7.3 Hz, 2H), 2.13−2.04 (m, 2H), 1.91−1.85 (m, 2H); MALDIFTMS (DHB) *m/z* 530.1838 ($M + H^+$, $C_{22}H_{26}F_3N_5O_7$ requires 530.1857).

Recombinant Human GAR Tfase Protein Preparation

The recombinant human GAR Tfase (purN) construct includes residues 808−1010 from the human trifunctional enzyme (purD-purM-purN). The gene was subcloned into the pet22b vector using the *Nde*I−*Xho*I cloning site with a hexahistidine tag at the C-terminus. The plasmid was transformed into *E. coli* expression strain BL21 (DE3) Gold. The protein was expressed and purified as described previously (*11*). The yield of the protein is greater than 30 mg/L of LB broth after purification, and at least 98% pure when assessed by SDS−PAGE. The purified protein was used in the inhibition assays, cytotoxic assays, and crystallization experiments.

GAR Tfase Inhibition Assay

The K_i values for the folate analogues were measured as previously described (*36*). Briefly, each compound was dissolved in dimethyl sulfoxide (DMSO) and then diluted in assay buffer. The low concentration of DMSO did not affect enzyme activity. Thus, all assays were conducted by mixing 10 μM 10-formyl-5,8-dideazafolate (fDDF) and 20 μM inhibitor in total volume of 1 mL of buffer [0.1 M HEPES (pH 7.5)] at 26 °C, and the reaction was initiated by the addition of 76 nM *E. coli* or human GAR Tfase. The assay monitors the deformylation of fDDF ($\Delta\epsilon$ = 18.9 mM^{-1} cm^{-1} at 295 nm) resulting from the transfer of the formyl group to β-GAR. If the inhibitor was found to be active, a series of $1/v_i$ versus 1/[GAR] at different, fixed concentrations of I (e.g., 4, 8, 12, 16, 20, and 32 μM) were generated to determine the K_i using the Michaelis−Menten equation for competitive inhibition.

Cytotoxic Assay

The cytotoxic activity of the compounds was measured using CCRF-CEM human leukemia cells, as described previously (*37*). Two mutant cell lines, CCRF-CEM/MTX and CCRF-CEM/FPGS$^-$, were used to determine the dependence on the reduced folate active transport system and folylpolyglutamate synthetase (FPGS), respectively (*38*).

Crystallization and Data Collection

Crystals of human GAR Tfase in complex with 10-CF_3CO-DDACTHF (**1**) were obtained by the method of vapor diffusion in 2 μL sitting drops. The protein solution, at a concentration of 16 mg/mL, was mixed with a 3-fold molar excess of the inhibitor. Needle-shaped crystals were obtained after 7 days at 4 °C from a solution of PEG4K, 0.2 M ammonium sulfate, and 50 mM HEPES (pH 6.7−7.0). Data were collected on an ADSC 2 × 2 CCD detector from a single crystal, cryoprotected by 20% glycerol at −179 °C on beamline 9-2 at the Stanford Synchrotron Radiation Laboratory (SSRL). The data set was processed with HKL2000 (*39*). The crystal space group is trigonal $P3_121$ with two molecules per asymmetric unit with a Matthews coefficient (*40*) of 4.5 $Å^3$ Da^{-1}, corresponding to a relatively high solvent content of 75%, consistent with the rather fragile crystals. The statistics for the data collection and processing are summarized in Table 1.

The human GAR Tfase complexed with 10-CF_3CO-DDACTHF (**1**) was also crystallized in MPEG5500 and 100

Table 1: Data Collection and Refinement Statistics

data reduction	
space group	$P3_121$
unit cell dimensions	$a = b = 126.24$ Å, $c = 94.42$ Å
no. of molecules per a.u.	2
resolution (Å)	45−1.98 (2.01−1.98)[a]
completeness (%)	99.7 (100)
multiplicity	3.9 (3.8)
average I/σ	24.9 (2.0)
R_{sym}[b] (%)	7.4 (60.1)
refinement	
data cutoff	$F_o > 0\sigma$
no. of reflections (test set)	57912 (2913)
no. of protein atoms	3016
no. of water molecules	251
no. of inhibitor atoms	76
average protein B value (Å^2)	33.1
average inhibitor B value (Å^2)	32.5
average solvent B value (Å^2)	36.8
rmsd from ideal	
bond lengths (Å)	0.014
bond angles (deg)	1.37
R_{cryst}[c] (%)	22.7
R_{free}[d] (%)	24.7
Ramachandran plot (%)	
most favored	92.6
additionally allowed	7.4

[a] Numbers in parentheses refer to the highest-resolution shell. [b] $R_{sym} = [\sum_h\sum_i|I_i(h) - \langle I(h)\rangle|/\sum_h\sum_i I_i(h)] \times 100$, where $\langle I(h)\rangle$ is the mean of the $I(h)$ observation of reflection. [c] $R_{cryst} = \sum_h||F_o| - |F_c||/\sum_h|F_o|$, where F_o and F_c are the observed and calculated structure factor amplitudes, respectively. [d] R_{free} (%) is the same as R_{cryst}, but for 5% of the data randomly omitted from refinement.

mM sodium acetate (pH 5.0−5.5) in trigonal space group $P3_1$ with a unit cell ($a = b = 126.07$ Å, $c = 94.02$ Å) similar to that of the pH 7.0 crystals, but with four molecules per asymmetric unit ($V_m = 4.5$ Å^3 Da^{-1}).

Structure Solution and Refinement

The crystal structure of human GAR Tfase in complex with 10-CF_3CO-DDACTHF (**1**) was determined by molecular replacement (MR) (*41*) using unliganded human GAR Tfase (PDB entry 1MEJ) as the search model in the program AmoRe from the CCP4 package (*42*). The initial refinement was carried out using the program CNS (*43*). The location of the folate inhibitor was clear in $F_o - F_c$ maps even after the first round of refinement. The inhibitor model was built into the electron density using O (*44*); strong density adjacent to the ketone oxygen suggested the hydrated form of the inhibitor was bound. Two-fold noncrystallographic restraints were used in the refinement of molecules A and B, except for flexible regions (residues 21−26, 58−63, 141−146, and 190−200) that have been seen to differ in other GAR Tfase structures. The final refinement was carried out using TLS refinement (*45*) from the CCP4 Refmac program. The final R_{cryst} and R_{free} values are 22.7 and 24.7%, respectively. The final model was evaluated by Procheck (*46*) and has 92.6% of the residues in the most favored regions of the Ramachandran plot with no outliers. Figures 3, 4, and 6 were created with Bobscript (*47*) and rendered with Raster3D (*48*). Figure 5 was generated with PMV (*49*). The final refinement statistics are presented in Table 1. Coordinates and structure factors have been deposited in the Protein Data Bank (*50*) as entry 1NJS.

Automated Docking of Cofactor

Two human and four *E. coli* templates of GAR Tfase for computational docking of the cofactor 10-formyl-THF were extracted from apo and ligand complex structures excluding the inhibitor coordinates. For human recombinant GAR Tfase, the published apo structure at pH 8.5 (PDB entry 1MEJ) and its complex with **1** were used for computer docking studies. For *E. coli* GAR Tfase, the apo structure at pH 7.5 (PDB entry 1CDE), and its complexes with BW1476U89 (PDB entry 1GAR), an epoxide-based inhibitor and substrate (PDB entry 1JKX), and 10-formyl-TDAF (**3**) and substrate (PDB entry 1C2T), were used for cofactor docking. Nonpolar hydrogens were merged with heavy atoms, and Kollman charges were assigned (*51*). His108 was fully protonated with a charge of +1 due to its reported high pK_a (*5*). 10-Formyl-THF was built and minimized with INSIGHTII (Molecular Simulations, Inc.). All-atom Gasteiger charges were added and nonpolar hydrogens merged (*52*). The native cofactor 10-formyl-THF was docked into the active site using AutoDock 3.0.5 (*53*, *54*), a suite of programs for automated docking of flexible ligands into protein targets. The docking simulations were performed using the Lamarkian genetic algorithm with a rapid grid-based lookup method for energy evaluation. The AutoTors utility of AutoDock was used to assign 11 rotatable bonds and 10 aromatic carbons in the ligand. Parameters for the docking were as follows: trials of 100, population size of 150, random starting position and conformation, translation step of 0.5 Å, rotation step of 15°, elitism of 1, mutation rate of 0.02, crossover rate of 0.8, local search rate of 0.06, and 50 million energy evaluations. Final docked conformations were clustered using a tolerance of 1.5 Å as the root-mean-square deviation (rmsd).

RESULTS AND DISCUSSION

Inhibitor Design. We have previously disclosed folate-based inhibitors that incorporate electrophilic functional groups that could potentially interact either with active site nucleophiles or with the GAR/AICAR substrate amine (*13*, *28*−*30*, *36*, *37*). The most significant of these were the folate-based inhibitor 10-formyl-TDAF (**3**) (*36*) and 10-formyl-DDACTHF (**4**) (*17*) bearing a nontransferable formyl group (Figure 1), which both proved to be potent GAR Tfase inhibitors. X-ray and NMR studies of the inhibitor−enzyme complexes revealed that the inhibitors bound as their gem-diols (*10*, *17*). The formation of the gem-diol mimics the formyl transfer tetrahedral intermediate and provides strong hydrogen bond interactions between the inhibitor and protein (*10*).

Even though 10-formyl-TDAF (**3**) was a relatively potent GAR Tfase inhibitor ($K_i = 260$ nM), it failed to exhibit effective cytotoxic activity that could be attributed to a combination of properties, including poor stability, ineffective transport by the reduced folate carrier, and inefficient intracellular polyglutamation by FPGS (*36*). In contrast, 10-formyl-DDACTHF (**4**), which replaces the quinazoline of **3** with a diaminopyrimidinone, is not only an effective GAR Tfase inhibitor but also a potent cytotoxic agent (CCRF-CEM $IC_{50} = 60$ nM) (*17*). Effective transport by the reduced folate carrier and efficient polyglutamation by FPGS were found to contribute to the cytotoxic activity by

enhancing its intracellular accumulation. Moreover, 10-formyl-DDACTHF (**4**) proved to be remarkably selective for human GAR Tfase (K_i = 14 nM against rhGAR Tfase) compared to *E. coli* GAR Tfase (K_i = 6 μM). Nevertheless, a facile oxidative decarbonylation of the key formyl group conveyed a chemical instability to **4**, precluding further consideration for *in vivo* use (*17*).

The use of trifluoromethyl ketones as reversible enzyme inhibitors has seen wide application, most notably in the field of serine proteases (*4*, *55*, *56*). In our continued evaluation of the GAR Tfase inhibitors, a trifluoromethyl ketone was introduced to replace the aldehyde of compound **4**. The trifluoromethyl ketone can serve to stabilize gem-diol formation of the electrophilic carbonyl to a greater extent than a formyl group and, hence, can promote active site binding by mimicking the tetrahedral intermediate of the formyl transfer reaction. By replacing N10 with a carbon, the inhibitor precludes formyl transfer yet can competitively bind to the folate-binding site (*17*, *36*). Such inhibitors display an enhanced affinity for folate-dependent enzymes involved in formyl transfer reactions, e.g., GAR Tfase and AICAR Tfase, and, therefore, exhibit selectivity toward these enzymes versus those involved in methyl or methylene transfer, such as thymidylate synthetase (TS).

Like **4**, analogue **1** was expected to be transported into cells by the reduced folate carrier and to be a substrate for FPGS, effectively sequestering it. It was also envisioned that **1** may exhibit enhanced chemical stability and pharmacological properties in comparison to aldehyde **4**. Thus, the evolution of compound **1** required assessment of a number of factors which include improved stability, the ability to enter cells by pathways involving the reduced folate carrier or folate-binding membrane protein transport system, efficient conversion within the cell to polyglutamated forms by FPGS, and optimization of the selectivity and affinity of the inhibitor for its target enzyme.

Inhibitor Synthesis and Chemical Characterization. The synthesis of **1** was accomplished as outlined in Figure 2. The known acid chloride **5** (*57*) was converted to the corresponding trifluoromethyl ketone **6** by reaction of trifluoroacetic anhydride (pyridine, CH_2Cl_2, −60 °C, 4 h) followed by aqueous quench (95%) (*58*, *59*). The ^{1}H NMR (CD_3OD) spectra of **6** clearly indicated peaks corresponding to the benzylic methylene protons at δ 3.34 and 3.1, as well as the absence of a peak corresponding to an enol methine, indicating that this compound exists as a hemiketal in CD_3OD, which was further corroborated by ^{13}C NMR (CD_3OD). Reaction of **6** with *N*,*N*-dimethylhydrazine (glacial AcOH, anhydrous EtOH, 25 °C, 48 h, 64%) provided the key *N*,*N*-dimethylhydrazone **7**. NaH deprotonation of **7** (DMF, 0 °C, 15 min) and subsequent treatment with excess 1,3-dibromopropane (6 equiv, DMF, 25 °C, 2.5 h, 65%) provided the monoalkylation product **8**. The preformed sodium salt of ethyl cyanoacetate (NaH, DMF, 0 °C, 30 min) was alkylated with **8** (DMF, 25 °C, 2 h) to give **9** (71%), and treatment with the free base of guanidine (1.2 equiv, CH_3OH, 25 °C, 1 h) under basic conditions gave the desired pyrimidinone **10** (Figure 2). Treatment of **10** with LiOH (3 equiv, 3:1 CH_3OH/H_2O, 25 °C, 24 h) cleanly hydrolyzed both the methyl ester and the dimethylhydrazone, providing **11**, which was coupled with di-*tert*-butyl L-glutamate hydrochloride (EDCI, $NaHCO_3$, DMF, 25 °C, 72 h) to provide

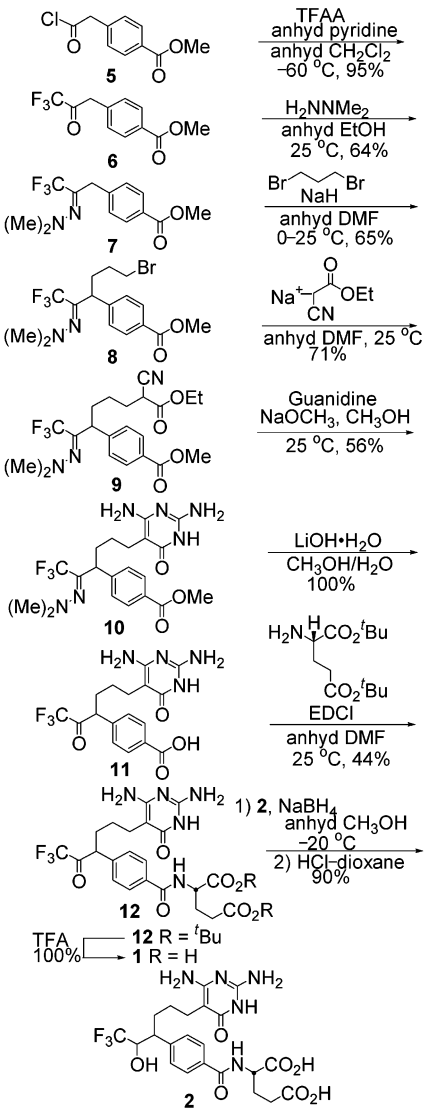

FIGURE 2: Synthesis of 10-CF_3CO-DDACTHF (**1**).

12. Deprotection of **12** was accomplished by treatment with trifluoroacetic acid [1/4 (v/v) TFA/$CHCl_3$, 25 °C, 12 h, 100%] to provide 10-CF_3CO-DDACTHF (**1**).

Most significantly, and unlike **3** and **4** which both suffer a facile oxidative decarbonylation reaction of the key formyl group (*17*, *36*), **1** was stable in pH 7−8 buffers in the presence of air, showing no decomposition or reaction after 7 days. When 10-CF_3CO-DDACTHF (**1**) was characterized by ^{1}H and ^{13}C NMR in CD_3OD, no ketone or enol form was observed, and **1** was found to be exclusively in the hemiacetal form. While this behavior is presumably solvent-dependent, these studies indicate that **1** likely exists in the hydrate form (gem-diol) in aqueous buffer and under the assay conditions. Finally, no evidence of separable C10 diastereomers was observed with **1**, indicating that the two diastereomers are in rapid equilibrium.

GAR Tfase Inhibition. 10-CF_3CO-DDACTHF (**1**) was assayed for inhibition of GAR Tfase and AICAR Tfase (Table 2) in comparison with other closely related folate-based GAR Tfase inhibitors. Compound **1** is a very effective inhibitor of rhGAR Tfase with a K_i of 15 nM. Significantly, the compound shows selectivity toward the human enzyme rather than the *E. coli* enzyme to which it is 100-fold less

Table 2: GAR and AICAR Tfase Inhibition (K_i, μM)

compound	*E. coli* GAR Tfase	rhGAR Tfase	rhAICAR Tfase
10-CF_3CO-DDACTHF (**1**)	1.9	0.015	>100
10-CF_3CHOH-DDACTHF (**2**)	20	0.900	>100
10-formyl-DDACTHF (**4**)	6	0.014	1
DDACTHF	5	1.7	nd[a]
Lometrexol	0.1	nd[a]	nd[a]

[a] Not determined.

Table 3: *In Vitro* Cytotoxic Activity[a]

compound	CCRF-CEM (IC_{50}, μM)			
	+T, +H	−T, +H	+T, −H	−T, −H
10-CF_3CO-DDACTHF (**1**)	>100	>100	0.017	0.016
10-CF_3CHOH-DDACTHF (**2**)	>100	>100	1.4	1.1
10-formyl-DDACTHF (**4**)	150	170	0.06	0.07
DDACTHF	>100	>100	3.6	2.7
Lometrexol	>100	>100	0.52	0.23
Methotrexate	0.05	0.05	0.04	0.04

[a] T is thymidine (10 μM), and H is hypoxanthine (100 μM).

potent with a K_i of 1.9 μM, consistent with past observations with rhGAR and *E. coli* GAR Tfase (*17*). **1** (K_i = 15 nM) proved to be roughly 60-fold more potent than the corresponding alcohol **2** (K_i = 900 nM) and 100-fold more potent than DDACTHF (K_i = 1.7 μM) lacking a C10 substituent altogether, indicating that each of the gem-diol alcohols contributes to active site binding. Inhibition was not tested for the trifunctional enzyme, but previous data have indicated that the recombinant human GAR Tfase has activity comparable to that of the intact human trifunctional enzyme (*7*, *11*, *60*).

10-CF_3CO-DDACTHF (**1**), as well as its corresponding alcohol **2**, is a specific inhibitor for GAR Tfase, but is inactive (K_i > 100 μM) against other folate-dependent enzymes, including AICAR Tfase, DHFR, and thymidylate synthetase (TS). These observations are consistent with the data below that show **1** derives its potent cytotoxic activity through inhibition of purine, not pyrimidine, biosynthesis and at a step preceding the action of AICAR Tfase.

Biological Activity. 10-CF_3CO-DDACTHF (**1**) and its corresponding alcohol **2** were examined for CCRF-CEM cytotoxic activity in the presence (+) and absence (−) of added hypoxanthine (purine) or thymidine (pyrimidine) (Table 3). Compound **1** exhibits potent cytotoxic activity (IC_{50} = 16 nM) against the CCRF-CEM cell line when purines (hypoxanthine) are absent in the medium. Moreover, it is ca. 14-fold more potent than Lometrexol (IC_{50} = 230 nM) and was inactive (IC_{50} > 100 μM) in the presence of medium purines. This sensitivity to the presence of purines, but not pyrimidines (thymidine), indicates that the cytotoxic activity of **1** is derived from inhibition of enzymes in the *de novo* purine biosynthetic pathway. To our knowledge, this places **1** among the most potent, if not the most potent, inhibitors of human GAR Tfase yet disclosed. The related alcohol **2** (IC_{50} = 1.1 μM) and DDACTHF lacking a C10 substituent (IC_{50} = 2.7 μM) also exhibited cytotoxic activity, which was also sensitive to the presence of medium purines. However, both are much less potent than ketone **1**.

AICAR rescue experiments were also performed with **1** and its corresponding alcohol **2** in an effort to further define the source of their cytotoxic activity. In each case, the reversal or rescue of the cytotoxicity with hypoxanthine (100 μM) or AICAR monophosphate (100 μM) resulted in an increase in the IC_{50} of 10^3-10^4 (data not shown). Thus, the observed activity is due to selective inhibition of purine biosynthesis prior to the AICAR Tfase enzymatic step, consistent with inhibition of GAR Tfase. This selective sensitivity to GAR Tfase is the expected behavior of inhibitors **1** and **2** based upon their inactivity against AICAR Tfase *in vitro*.

The extent to which the cytotoxic activity of **1** and **2** was dependent on reduced folate transport across the cellular membrane was established by assaying against a mutant CCRF-CEM cell line (CEM/MTX) (*60*) which is deficient in the reduced folate carrier. Like Lometrexol, **1** and the related hydroxyl compound **2** lost activity against CCRF-CEM/MTX (data not shown), indicating the reduced folate carrier is required for activity and implying that they are effective substrates for transport.

Similarly, the importance of FPGS polyglutamation to cytotoxic activity was established by examining the inhibitor against a CCRF-CEM cell line deficient in FPGS (CCRF-CEM/FPGS$^-$) (*17*). Like Lometrexol, **1** and the related hydroxyl compound **2** (to a lesser extent) lacked or lost activity against this cell line (data not shown), indicating polyglutamation is required for activity of the inhibitors, presumably by directly enhancing enzyme inhibitory activity and/or as a consequence of intracellular accumulation of the inhibitors by preventing diffusion out of the cell.

X-ray Structure Determination. The crystal structure of rhGAR Tfase, cocrystallized with **1** at physiological pH (pH 7), was determined at 1.98 Å resolution by MR using the unliganded human GAR Tfase at pH 8.5 (PDB entry 1MEJ) as the search model (Figure 3A). The crystal space group is $P3_121$ with two molecules per asymmetric unit, but no dimeric interaction is observed, consistent with other structures of human GAR Tfase, in which the enzyme always crystallizes as a monomer. The two monomers have very similar structures (main chain rmsd of 0.4 Å), and each contains a bound inhibitor **1** in the folate-binding site (Figure 3A). The final model of the complex includes residues 808−1007 from the trifunctional protein, with the last three residues not interpretable due to disorder. The numbering of the residues is the same as that for unliganded human GAR Tfase (*11*).

A preliminary 1.8 Å resolution structure has been obtained for human GAR Tfase bound to 10-CF_3CO-DDACTHF (**1**) at pH 5. The only major difference is the previously observed conformational isomerism in the substrate binding pocket, in which the pocket is not accessible to the substrate at pH 5, but is open at pH 7 (*11*). The folate-binding site is identical in the two structures (main chain rmsd of the folate-binding loop of residues 140−146 = 0.08 Å).

Overall Structure. The overall topology of the complex between human GAR Tfase and 10-CF_3CO-DDACTHF (**1**) is very similar to that of the unliganded protein structure at pH 8.5 (PDB entry 1MEJ) (Figure 3A) (rmsd of 0.86 and 0.89 Å for molecules A and B, respectively). Molecule B has slightly higher thermal factors (average B of 35.3 Å^2) than molecule A (average B of 31.0 Å^2) (Table 4). The loop helix of residues 110−131 is highly ordered in the complex structure (B value of 24.5 Å^2), consistent with our previous

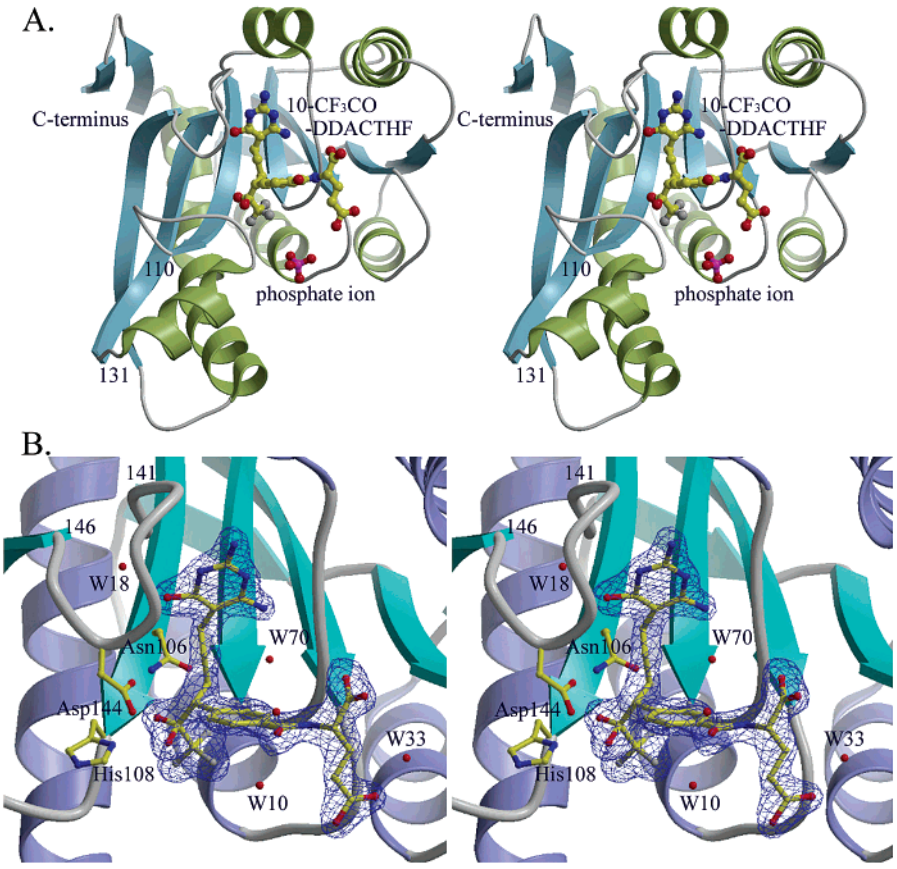

FIGURE 3: Crystal structure of the human GAR Tfase−10-CF_3CO-DDACTHF (**1**) complex. (A) Stereoview of the overall topology of the complex illustrated by a ribbon diagram with helices shown as coils in green and strands as extended arrows in sky blue. The inhibitor 10-CF_3CO-DDACTHF (**1**) and phosphate ion are represented in ball-and-stick format with the oxygen atoms colored red, nitrogens blue, fluorides gray, phosphates purple, and carbons yellow. (B) Inhibitor bound in the folate-binding site. The $2F_o - F_c$ electron density map of the inhibitor 10-CF_3CO-DDACTHF (**1**) is contoured at 2σ. The inhibitor, catalytic residues, and ordered water molecules in the inhibitor binding site are illustrated in ball-and-stick format using the same color scheme as in panel A.

Table 4: *B* Value Comparison of Unliganded Human GAR Tfase, *E. coli* GAR Tfase in Complex with 10-Formyl-TDAF and Substrate, and Human GAR Tfase in Complex with 10-CF_3CO-DDACTHF (**1**)

	human complex with 10-CF_3CO-DDACTHF (**1**)		*E. coli* complex with 10-formyl-TDAF and β-GAR	unliganded human form
	molecule 1 (Å^2)	molecule 2 (Å^2)	(Å^2)	(Å^2)
protein	31.0	35.3	29.6	30.1
inhibitor	25.8	39.3	43.5	–
residues 110−131	22.4	26.6	41.1	23.6
residues 141−146	30.0	37.5	45.4	64.4

result that this loop helix maintains a uniform conformation in human GAR Tfase (*11*), unlike the pH-dependent order−disorder transition in the *E. coli* enzyme (Table 4). As substrate β-GAR was not present in the crystallization screens, the substrate-binding site was occupied by an inorganic phosphate ion (Figure 3A). Unlike the *E. coli* complex structures and unliganded human GAR Tfase in which the folate-binding loop of residues 141−146 has very high *B* values, the same loop in the human enzyme has *B* values (33.8 Å^2) comparable to that of the overall structure (33.0 Å^2) (Table 4) when bound to the inhibitor.

The inhibitor binds in the folate-binding site with strong, clear, and interpretable density (Figure 3B) with *B* values similar to those of the neighboring protein atoms, indicating full occupancy within the binding site. This first complex structure of GAR Tfase with only a cofactor analogue bound helps to elucidate a puzzle unresolved from many prior complex structures of the *E. coli* enzyme in which folate analogues do not produce GAR Tfase complex crystals in the absence of substrate (*10*). This crystallization observation is not only inconsistent with kinetic results that suggest inhibitors bind to GAR Tfase in both the presence and absence of substrate β-GAR (*6*, *17*, *36*) but also at odds with the sequential binding mechanism proposed for the mammalian trifunctional GAR Tfase enzyme in which the cofactor binds first (*7*, *62*).

Inhibitor Binding. The cofactor binding pocket of GAR Tfase is located at the interface between the N-terminal mononucleotide binding domain and the C-terminal half of the structure (Figure 3A). Only the *R* form of compound 10-CF_3CO-DDACTHF is found in the folate-binding site (Figure 3B), as compared to the complex of 10-formyl-TDAF with *E. coli* GAR Tfase and substrate (PDB entry 1C2T), in which both *R* and *S* diastereomers can be modeled into the electron density (*10*). The binding site for the folate cofactor moiety consists of three parts: the pteridine binding cleft, the benzoylglutamate region, and the formyl transfer region (Figure 4A).

(1) Pteridine Binding Cleft. The diaminopyrimidinone ring of **1** is deeply buried in the active site cleft and occupies the same location as the quinazoline ring of 10-formyl-TDAF

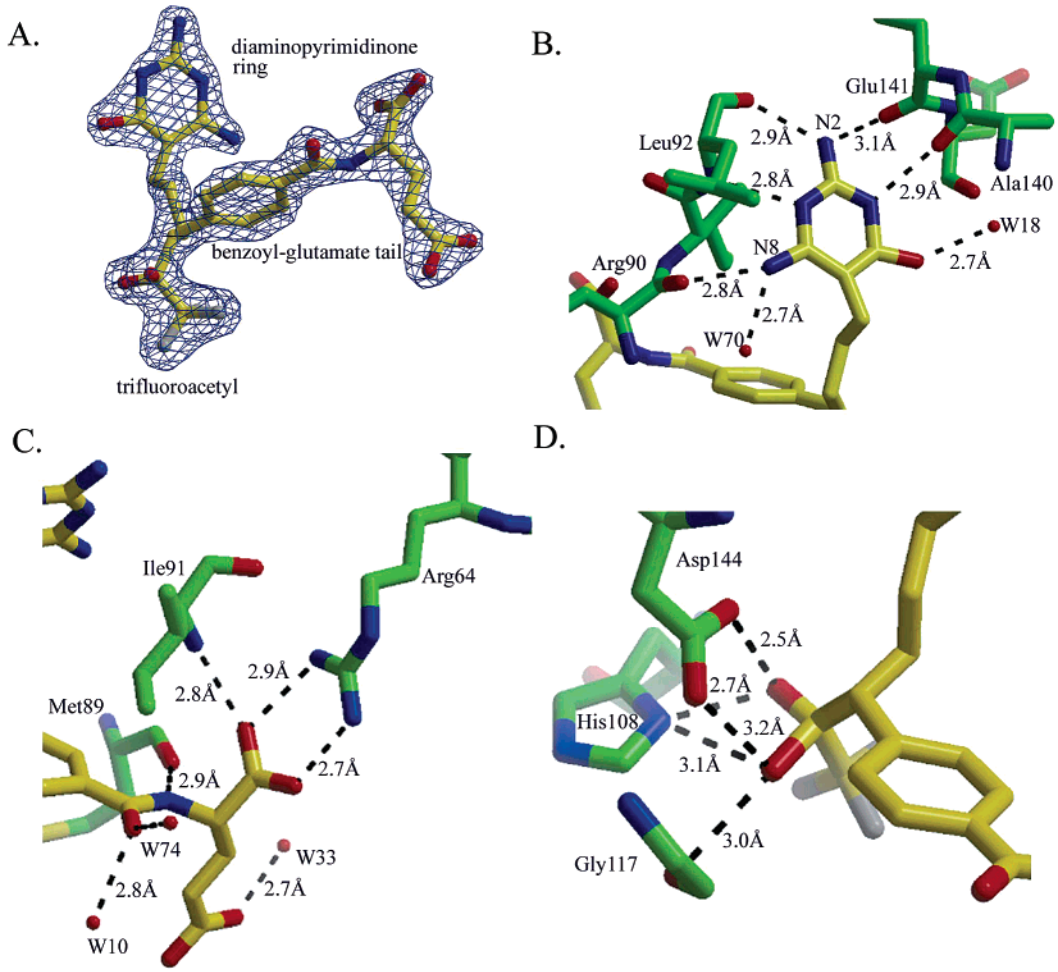

FIGURE 4: Human GAR Tfase−10-CF_3CO-DDACTHF (**1**) interaction. (A) The final refined model of inhibitor **1** is superimposed on the $2F_o - F_c$ electron density contoured at 2σ. The key interactions of the inhibitor and human GAR Tfase are between the protein side chains and three moieties of the inhibitor: diaminopyrimidinone ring, trifluoroacetyl group, and benzoyl glutamate tail. (B) Interaction between the diaminopyrimidinone ring of inhibitor **1** and GAR Tfase. Protein side chains and the inhibitor atoms are represented in ball-and-stick format using the same color scheme as in Figure 3, except for the carbon atoms of protein which are colored green, while bonds and carbon atoms in the inhibitor are colored yellow. The potential hydrogen bonds are drawn using dashed lines with the distances in angstroms. (C) Interaction between the glutamate tail of inhibitor **1** and the protein. The representation and color scheme are the same as in panel B. (D) Interaction between the gem-diol of the inhibitor and the protein. Extensive hydrogen bonding interactions are formed between the gem-diol of inhibitor **1** and catalytic residues His108 and Asp144.

(**3**) in the *E. coli* GAR Tfase complex (PDB entry 1C2T). The connecting stem from the diaminopyrimidinone ring, composed of single carbon bonds, is longer than its counterpart in 10-formyl-TDAF (**3**), due to the removal of the fused benzene ring, which makes it more flexible when adapting to the binding site to optimize the gem-diol interactions with the protein. The diaminopyrimidinone ring of **1** is tilted ~15° relative to the quinazoline ring of **3**, which places N2 within hydrogen bonding range (3.1 Å) of the backbone carbonyl oxygen of Glu141 (Figure 4B). The diaminopyrimidinone ring conserves all of the key interactions that were previously observed with the quinazoline ring of **3**, and provides additional key hydrogen bonds with the enzyme. Several hydrophobic residues encircle a deep cavity holding the heterocycle. The hydrophobic pocket consists of Leu85, Ile91, Leu92, Phe96, and Val97 lining one end and the folate-binding loop of residues 141−146 at the other. The diaminopyrimidinone ring makes six hydrogen bonds to the main chain amides and carbonyls of Arg90, Leu92, Ala140, Glu141, and Asp144, and two hydrogen bonds to ordered waters (W18 and W70) (Figure 4B).

In the quinazoline ring of 10-formyl-TDAF (**3**), N8 of the folate pteridine ring is replaced with a carbon. This nitrogen has been proposed to play a key role in recognition and interaction with folate-binding enzymes and forms one end of an H-bond donor−acceptor−donor array. While its replacement with carbon does not preclude the binding to GAR Tfase, its presence appears to contribute to substrate recognition by the folate transport system and/or FPGS (*17*). The diaminopyrimidinone ring of **1**, however, preserves this nitrogen (N8) and, consequently, exhibits superb biological properties. In the 10-CF_3CO-DDACTHF complex, this amino group forms hydrogen bonds to the carbonyl oxygen of Arg90 (2.8 Å) and an ordered solvent molecule W70 (2.7 Å) (Figure 4B).

(2) Glutamate Tail. The role of the benzoylglutamate group of the folate is not yet fully understood. However, the 10-CF_3CO-DDACTHF **1** compound without the benzoyl-glutamate tail is inactive against both GAR Tfase and AICAR Tfase (T. H. Marsilje et al., *Bioorg. Med. Chem.*, in press. In the 10-CF_3CO-DDACTHF complex, the *p*-aminobenzoate moiety is located in a hydrophobic pocket sandwiched

between the side chains of Ile91 and Ser118. The electron density of the carbonyl group is well-defined and in the same plane as the phenyl ring. The glutamate tail is oriented almost perpendicular to the *p*-aminobenzoate plane and parallel to the aliphatic stem of the diaminopyrimidinone ring (Figure 4A).

In *E. coli*, two distinct polyglutamation activities involve amide linkage through either α- or γ-carboxylates. The first two L-glutamate additions are catalyzed by dihydrofolate synthetase-folylpolyglutamate synthetase to the γ-carboxylate (*34*). Glutamate residues 4−8 are then linked to the polyglutamate chain at the α-carboxylate by another enzyme, folylpoly-α-glutamate synthetase (*35*). This issue is simplified in eukaryotes where all the glutamates are added at the γ-carboxylate of the previous glutamate by a single enzyme, FPGS (*31*).

The monoglutamate tail of the antifolates in the previous structural studies with *E. coli* GAR Tfase is highly flexible, as indicated by high *B* values. Alternative conformations of this tail have been observed, suggesting that the tail can flip between two distinct conformations when it is a monoglutamate. In the BW1476U89 (*8*) and 10-formyl-TDAF (**3**) complexes (*10*), the γ-glutamate carboxylate forms a salt bridge with Arg64, and the α-carboxylate points out (Figure 5A). However, in the epoxide-derived folate analogue complex structure (PDB entry 1JKX) (*63*), the α-glutamate carboxylate forms the salt bridge with the *E. coli* enzyme instead. In some cases, no obvious preferred binding orientation is observed; therefore, the glutamate tail tends to becomes disordered in these crystal structures, as in the DATHF and *E. coli* GAR Tfase complex (*9*).

In this complex structure of compound **1** with human GAR Tfase, the glutamate moiety is solvent-exposed, as expected, but exhibits a remarkably well-ordered structure (Figure 4A), in contrast to its flexibility in *E. coli* GAR Tfase complex structures. A single glutamate can contribute substantially to tight binding as indicated by the lack of inhibition of analogue **1** without the glutamate (compound **11**) for rhGAR Tfase (data not shown). A salt bridge (2.7 Å) is formed (Figure 4C) between the glutamate α-carboxylate and Arg64 so that the γ-carboxylate points to the solvent (Figure 5B). An additional interaction observed here includes a hydrogen bond between the Ile91 backbone amide and the α-glutamate carboxylate (2.8 Å) (Figure 4C).

(3) Formyl Transfer Region and the Gem-Diol Structure. Key interactions for tight binding of inhibitor **1** to GAR Tfase are found in the formyl transfer region. Strong density next to the ketone oxygen indicates that the ketone is hydrated to a gem-diol, similar to the 10-formyl-TDAF and β-GAR complex with the *E. coli* GAR Tfase (PDB entry 1C2T).

The gem-diol forms extensive interactions with the formyl transfer region, especially with Asp144 and His108, two essential residues in the formyl transfer reaction (Figure 4D). The Asp144 carboxylate hydrogen bonds (2.5 and 2.7 Å) to each of the hydroxyl groups of the gem-diol. N3 in the imidazole ring of His108 also forms hydrogen bonds with both hydroxyls of the gem-diol [OA1 (2.7 Å) and OA2 (3.1 Å)]. Additionally, OA2 also makes a potential hydrogen bond (3.0 Å) with the backbone carbonyl oxygen of Gly117. This extensive hydrogen bonding interaction between the enzyme and the inhibitor explains why the corresponding

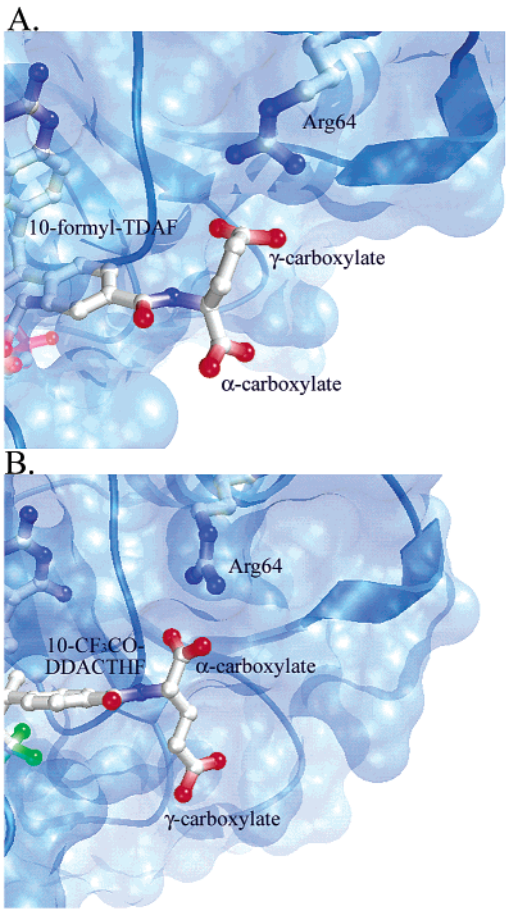

FIGURE 5: Orientation of the glutamate tails of folate analogues in complex with *E. coli* and human GAR Tfase. The translucent solvent accessible surface is superimposed on the ribbon diagram of the protein. (A) γ-Carboxylate binding of the glutamate tail to *E. coli* GAR Tfase. The structure represents the complex structure of *E. coli* GAR Tfase with 10-formyl-TDAF and β-GAR (PDB entry 1C2T). A salt bridge is formed between Arg64 and the γ-carboxylate so that the α-carboxylate is exposed to solvent. (B) α-Carboxylate binding of the glutamate tail to human GAR Tfase. The structure represents the human GAR Tfase complex with **1**. The salt bridge is now between Arg64 and the α-carboxylate so that its γ-carboxylate is exposed to solvent.

alcohol (Figure 1, compound **2**) of the 10-CF_3CO-DDACTHF, which lacks one of the hydroxyl groups, is ca. 60 times less potent.

Folate-Binding Loop. One of the main challenges of inhibitor design for GAR Tfase is the structural isomerism of the folate-binding loop of residues 141−146, which contains a key residue (Asp144) for formyl transfer. Under different conditions, this loop shows a variety of conformations (*8*, *10*, *11*, *63*, *64*) (Figure 6A). For example, in the obligate monomeric mutant (E70A) of *E. coli* GAR (PDB entry 2GAR) (*64*) at pH 3.5, this loop folds into the folate-binding pocket (closed conformation) and occupies the folate binding position (Figure 6A), whereas at pH 7.5 (PDB entry 3GAR) (*64*), it moves away so that the binding pocket is accessible to folate or folate analogues (Figure 6A). In the *E. coli* GAR Tfase complex with 10-formyl-TDAF (**3**) and substrate (PDB entry 1C2T) (*10*), the folate-binding loop stabilizes the gem-diol structure through hydrogen bonds between Asp144 and the hydrated aldehyde. In an epoxide-derived analogue complex (PDB entry 1JKX), the loop has yet another conformation (Figure 6A) where Asp144 interac-

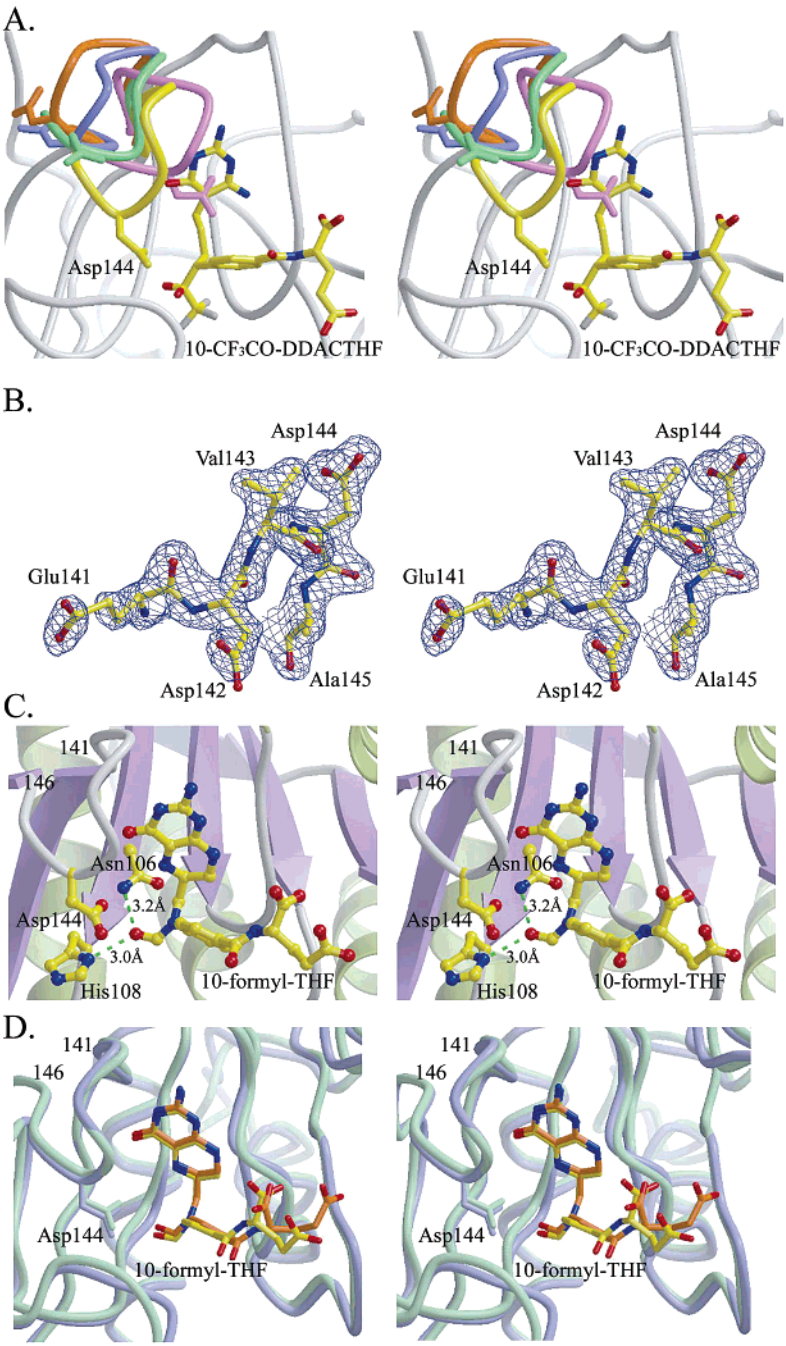

FIGURE 6: GAR Tfase folate-binding loop. (A) Structural isomerism of the folate-binding loop of residues 141−146. The structure of the 10-CF_3CO-DDACTHF (**1**) complex is colored gray, except for residues 141−146 which are colored yellow. The loops from different *E. coli* and human structures are superimposed onto the human GAR Tfase−**1** complex with Asp144 shown in ball-and-stick format. This loop in high-pH *E. coli* mutant E70A (PDB entry 3GAR) is colored orange, unliganded human GAR Tfase at pH 8.5 (PDB entry 1MEJ) blue, dibromide folate analogue in complex with *E. coli* GAR Tfase (PDB entry 1JKX) green, and low-pH *E. coli* mutant E70A (PDB entry 2GAR) in pink. The inhibitor 10-CF_3CO-DDACTHF (**1**) is represented in ball-and-stick format. (B) The folate-binding loop in human GAR Tfase becomes ordered upon binding of inhibitor **1**. The $2F_o - F_c$ electron density map of the loop is contoured at 2σ with refined coordinates superimposed in ball-and-stick format. (C) Docking interaction of the natural cofactor folate with human GAR Tfase. The catalytic triad (Asn106, His108, and Asp144) are in the proximity of the formyl group of the cofactor to facilitate the formyl transfer reaction. (D) Superposition of human GAR Tfase (human GAR Tfase−**1** complex as the template) and *E. coli* GAR Tfase (PDB entry 1C2T) docked with the natural folate cofactor. The lowest-energy clusters in both cases share substantial similarities in both protein and cofactor conformation. The protein main chain is illustrated by a tube with the human enzyme colored blue and the *E. coli* enzyme green. The docked cofactors are represented in ball-and-stick format using a color scheme similar to that in Figure 3. The carbon skeleton of the docked cofactor using the human GAR Tfase template is colored yellow, while the carbons of the folate using the *E. coli* template are colored orange.

tions are mediated via a cluster of ordered solvent molecules (*63*), instead of direct hydrogen bonds to the inhibitor.

In unliganded human GAR Tfase (PDB entry 1MEJ) at pH 8.5, this loop is "half-open", but at pH 4.2 (PDB entry 1MEO), these residues are disordered (*11*) (Figure 6A). These multiple conformations in which residues 141−146 have very high *B* values, or are disordered, make determining which structure is optimal for computational calculations and

Table 5: Docking of the Folate Cofactor into Human and *E. coli* GAR Tfase Structures

	no. of clusters	percentage of conformers in the lowest cluster	docking *E* (kcal/mol)	binding *E* (kcal/mol)
human recombinant form				
1	6	49	−19.0	−15.5
apo (1MEJ)	11	15	−16.4	−13.1
E. coli form				
3 with β-GAR (1C2T)	2	38	−17.7	−14.5
BW1476U89 (1GAR)	1	100	−16.9	−13.2
epoxide with β-GAR (1JKX)	3	68	−15.5	−12.2
apo (1CDE)	18	22	−13.9	−11.0

docking studies problematic. However, this flexible loop is stabilized in the human GAR Tfase upon the binding of the folate analogue, 10-CF_3CO-DDACTHF (Figure 6B). The loop exhibits excellent density with a *B* value (33.8 Å^2) comparable to that of the overall enzyme (33.0 Å^2) (Table 4), and has a conformation identical to that of the *E. coli* enzyme complex with 10-formyl-TDAF, except for the orientation of the side chains of Glu141, Asp142, and Val143.

These changes in the loop conformation help provide most of the inhibitor interactions with the enzyme. The backbone carbonyl oxygens of Glu141 and Asp144 are involved in directly anchoring the diaminopyrimidinone ring, whereas a water molecule (W18 in molecule A and W27 in molecule B) mediates interactions between the backbone amide and carbonyls of the folate-binding loop and the diaminopyrimidinone ring. But most importantly, Asp144 at the tip of the loop provides a key interaction with the inhibitor. The side chain of Asp144 rotates ~90° (rmsd of 5.5 Å, in comparison to the unliganded human GAR Tfase structure) and flips into the folate-binding pocket to form hydrogen bonds with the gem-diol (Figure 6A), putting it in the vicinity of His108 (Figure 6C). Contrary to the flexible Asp144, His108 is tightly anchored by its interaction with the main chain carbonyl oxygen of Lys115 (2.8 Å) and the hydroxyl of Ser110 (3.0 Å). The translocation of Asp144 facilitates formation of a salt bridge with His108, which appears to be essential for the formyl transfer reaction (*6*). The highly ordered folate-binding loop and its extensive interactions with the inhibitor suggest that this structure is an excellent template for computational docking.

Docking of the Folate Cofactor. The natural cofactor 10-formyl-THF is unstable and not ideal for cocrystallization studies. Therefore, computational docking was used to probe the interaction between the enzyme and natural cofactor. Using the coordinates of the human GAR Tfase complex with 10-CF_3CO-DDACTHF, six docking clusters were obtained. The lowest-energy cluster with a docking energy of −19.0 kcal/mol and a binding energy of −15.5 kcal/mol is also the largest, representing almost half (49%) of all the conformers (Table 5). In contrast, as many as 11 clusters were obtained with apo human GAR Tfase (PDB entry 1MEJ), with the most dominant cluster representing only 15% of the conformers, with a much less favorable docking energy (−16.4 kcal/mol) (Table 5). Furthermore, when docked with the apo human GAR Tfase template, the pteridine ring is inserted between the folate-binding loop (residues 141−146) and His108, contradicting published kinetic and structural data. In the best conformer of the cofactor with the rhGAR Tfase−10-CF_3CO-DDACTHF (**1**) complex as a template, the formyl group hydrogen bonds to His108 (3.0 Å) and Asn106 (3.2 Å), with Asp144 in the vicinity, potentially stabilizing the protonation of His108 (Figure 6C). This conformation of the docked folate cofactor strongly supports the proposed mechanism (*6*, *64*). The rhGAR Tfase−10-CF_3CO-DDACTHF (**1**) template then is much more appropriate for mechanistic studies and structurally based drug design.

To compare folate binding to both human and *E. coli* GAR Tfases, a comprehensive docking analysis was performed on four different *E. coli* GAR Tfase structures (Table 5). The cluster with the lowest docking (−17.7 kcal/mol) and binding energy (−14.5 kcal/mol) was observed with the *E. coli* GAR Tfase complex with 10-formyl-TDAF (**3**) and substrate β-GAR (PDB entry 1C2T). With the multisubstrate adduct complex (PDB entry 1GAR), BW1476U89, only one cluster was obtained. However, the covalent carbon and sulfur linker between the folate and substrate moieties of the inhibitor may distort the active site, resulting in a less favorable docking energy (docking $E = -16.9$ kcal/mol). Similarly, the epoxide-derived inhibitor complex (PDB entry 1JKX) is also less favorable as a template (docking $E = -15.5$ kcal/mol). The worst case was found for apo *E. coli* GAR Tfase, with a scattering of 18 clusters, none of which has a reasonable folate-binding position, with a docking energy of only −13.9 kcal/mol for the lowest-energy cluster. In this case, the docked folate pteridine ring reverses its position and binds to the substrate-binding pocket, which obviously contradicts the folate analogue and *E. coli* GAR Tfase complex structures.

Comparison of the best docking results from the various human and *E. coli* GAR Tfase structures (rhGAR Tfase−10-CF_3CO-DDACTHF and eGAR Tfase−10-formyl-TDAF−β-GAR templates, respectively) shows that the folate-binding site and the folate cofactor have similar conformations (Figure 6D). Slight differences (rmsd of 0.4 Å for residues 140−146) are mostly caused by the higher flexibility of this loop in the *E. coli* structures. For the folate cofactor, the pteridine ring forms hydrogen bonds mainly to the protein backbone. The formyl group is close to His108, Asp144, and Asn106, the formyl transfer catalytic triad (Figure 6C). The docking confirms that His108, Asp144, and Asn106 are central to the enzyme formyl transfer reaction.

CONCLUSIONS

The work presented here represents a complete structure-based drug design cycle for GAR Tfase: structure, analysis, synthesis, and evaluation that then returns to structure. Our previous structure of *E. coli* GAR Tfase in complex with

the cofactor analogue 10-formyl-TDAF and substrate β-GAR (PDB entry 1C2T) revealed that the inhibitor bound as a hydrated gem-diol, interacting with the enzyme in a manner that mimics that of the formyl transfer intermediate (*10*). On the basis of this structural insight, a new compound 10-CF_3CO-DDACTHF (**1**) was designed and synthesized to facilitate and stabilize the formation of a gem-diol in the binding site. The newly designed compound was found to be a selective and unusually effective inhibitor of rhGAR Tfase, representing the most potent folate analogue described to date. In addition, **1** was inactive against AICAR Tfase, TS, and DHFR. This compound acts as a surrogate cofactor, but is incapable of formyl transfer. Its structural resemblance to the natural folate cofactor suggested that it might be accepted as a substrate for cellular folate transport systems, as well as for FPGS, as confirmed by cytotoxic assays. Most importantly, the compound is chemically stable. All these properties make this compound a potential lead for *in vivo* studies of it as a chemotherapeutic agent.

This compound was crystallized with rhGAR Tfase and its structure compared to an *E. coli* structure with a related folate analogue, 10-formyl-TDAF (**3**) (*10*). The folate-binding loops of these two structures are very similar with a few minimal differences for the side chains of Glu141, Asp142, and Val143, most likely caused by the higher flexibility of this loop in the *E. coli* structure. Although other important differences have been found between the structures of bacterial and human GAR Tfases, the folate-binding pocket conformations share a high degree of resemblance so that information obtained from this particular *E. coli* GAR complex was invaluable for inhibitor design.

The availability now of unliganded and inhibitor-bound human GAR Tfase structures at high resolution reveals subtle changes upon inhibitor binding. The most dramatic change takes places in the folate-binding loop of residues 141−146, which forms key interactions with the inhibitor. This conformational change juxtaposes Asp144 and the tightly anchored His108 and Asn106. As His108 and Asn106 have consistent locations and conformations in various structures, the translocation of Asp144 upon inhibitor binding finally assembles the complete reaction triad within one structure into a configuration that is presumably ready for catalysis and proton shuffling in the formyl transfer reaction.

The coordinates of the rhGAR Tfase−10-CF_3CO-DDACTHF (**1**) complex provide a much better model than apo human GAR Tfase for docking simulations of the natural folate cofactor. The less favorable energy for docking to the apoprotein and the inappropriate positioning of the folate cofactor in this structure suggest that the folate-binding loop undergoes a conformational change to accommodate the folate or folate analogue, probably by induced fit. For both human and *E. coli* GAR Tfases, one particular conformation of the folate-binding loop is found to be the most energetically favorable, suggesting that the crystal structure of rhGAR Tfase in complex with 10-CF_3CO-DDACTHF provides a reasonable "snapshot" of its interaction with the natural folate cofactor. These combined crystallographic and computational studies greatly enhance our understanding of the GAR Tfase formyl transfer mechanism and the design of subsequent generations of GAR Tfase inhibitors.

ACKNOWLEDGMENT

We thank X. Dai for help with data collection and processing, N. Larsen, A. Heine, and X. Zhu for valuable suggestions, M. Elsliger for computational assistance, and the staff of SSRL beamline 9-2 for technical support during X-ray data collection.

REFERENCES

1. Dev, I. K., and Harvey, R. J. (1978) *J. Biol. Chem. 253*, 4242−4244.
2. Caperelli, C. A. (1989) *J. Biol. Chem. 264*, 5053−5057.
3. Inglese, J., Johnson, D. L., Shiau, A., Smith, J. M., and Benkovic, S. J. (1990) *Biochemistry 29*, 1436−1443.
4. Wolfenden, R. (1976) *Annu. Rev. Biophys. Bioeng. 5*, 271−306.
5. Shim, J. H., and Benkovic, S. J. (1998) *Biochemistry 37*, 8776−8782.
6. Shim, J. H., and Benkovic, S. J. (1999) *Biochemistry 38*, 10024−10031.
7. Poch, M. T., Qin, W., and Caperelli, C. A. (1998) *Protein Expression Purif. 12*, 17−24.
8. Klein, C., Chen, P., Arevalo, J. H., Stura, E. A., Marolewski, A., Warren, M. S., Benkovic, S. J., and Wilson, I. A. (1995) *J. Mol. Biol. 249*, 153−175.
9. Almassy, R. J., Janson, C. A., Kan, C. C., and Hostomska, Z. (1992) *Proc. Natl. Acad. Sci. U.S.A. 89*, 6114−6118.
10. Greasley, S. E., Yamashita, M. M., Cai, H., Benkovic, S. J., Boger, D. L., and Wilson, I. A. (1999) *Biochemistry 38*, 16783−16793.
11. Zhang, Y., Desharnais, J., Greasley, S. E., Beardsley, G. P., Boger, D. L., and Wilson, I. A. (2002) *Biochemistry 41*, 14206−14215.
12. Taylor, E. C., Harrington, P. J., Fletcher, S. R., Beardsley, G. P., and Moran, R. G. (1985) *J. Med. Chem. 28*, 914−921.
13. Boger, D. L., Haynes, N. E., Warren, M. S., Ramcharan, J., Kitos, P. A., and Benkovic, S. J. (1997) *Bioorg. Med. Chem. 5*, 1839−1846.
14. Boger, D. L., Haynes, N. E., Warren, M. S., Ramcharan, J., Kitos, P. A., and Benkovic, S. J. (1997) *Bioorg. Med. Chem. 5*, 1853−1857.
15. Boger, D. L., Haynes, N. E., Warren, M. S., Gooljarsingh, L. T., Ramcharan, J., Kitos, P. A., and Benkovic, S. J. (1997) *Bioorg. Med. Chem. 5*, 1831−1838.
16. Varney, M. D., Palmer, C. L., Romines, W. H., III, Boritzki, T., Margosiak, S. A., Almassy, R., Janson, C. A., Bartlett, C., Howland, E. J., and Ferre, R. (1997) *J. Med. Chem. 40*, 2502−2524.
17. Marsilje, T. H., Labroli, M. A., Hedrick, M. P., Jin, Q., Desharnais, J., Baker, S. J., Gooljarsingh, L. T., Ramcharan, J., Tavassoli, A., Zhang, Y., Wilson, I. A., Beardsley, G. P., Benkovic, S. J., and Boger, D. L. (2002) *Bioorg. Med. Chem. 10*, 2739−2749.
18. Newell, D. R. (1999) *Semin. Oncol. 26*, 74−81.
19. Takimoto, C. H. (1997) *Semin. Oncol. 24*, A18-40−S18-51.
20. Beardsley, G. P., Moroson, B. A., Taylor, E. C., and Moran, R. G. (1989) *J. Biol. Chem. 264*, 328−333.
21. Laohavinij, S., Wedge, S. R., and Lind, M. J. (1996) *Invest. New Drugs 14*, 325−335.
22. Roberts, J. D., Poplin, E. A., and Tombes, M. B. (2000) *Cancer Chemother. Pharmacol. 45*, 103−110.
23. Schild, D., Brake, A. J., Kiefer, M. C., Young, D., and Barr, P. J. (1990) *Proc. Natl. Acad. Sci. U.S.A. 87*, 2916−2920.
24. Daubner, S. C., Young, M., Sammons, R. D., Courtney, L. F., and Benkovic, S. J. (1986) *Biochemistry 25*, 2951−2957.
25. Aimi, J., Qiu, H., Williams, J., Zalkin, H., and Dixon, J. E. (1990) *Nucleic Acids Res. 18*, 6665−6672.
26. Inglese, J., Smith, J. M., and Benkovic, S. J. (1990) *Biochemistry 29*, 6678−6687.
27. Warren, M. S., Marolewski, A. E., and Benkovic, S. J. (1996) *Biochemistry 35*, 8855−8862.
28. Boger, D. L., Kochanny, M. J., Cai, H., Wyatt, D., Kitos, P. A., Warren, M. S., Ramcharan, J., Gooljarsingh, L. T., and Benkovic, S. J. (1998) *Bioorg. Med. Chem. 6*, 643−659.
29. Boger, D. L., Marsilje, T. H., Castro, R. A., Hedrick, M. P., Jin, Q., Baker, S. J., Shim, J. H., and Benkovic, S. J. (2000) *Bioorg. Med. Chem. Lett. 10*, 1471−1475.
30. Boger, D. L., Labroli, M. A., Marsilje, T. H., Jin, Q., Hedrick, M. P., Baker, S. J., Shim, J. H., and Benkovic, S. J. (2000) *Bioorg. Med. Chem. 8*, 1075−1086.

31. Moran, R. G. (1983) *Adv. Exp. Med. Biol. 163*, 327−339.
32. Shane, B., Bognar, A. L., Goldfarb, R. D., and LeBowitz, J. H. (1983) *J. Bacteriol. 153*, 316−325.
33. McGuire, J. J., Hsieh, P., and Bertino, J. R. (1984) *Biochem. Pharmacol. 33*, 1355−1361.
34. Ferone, R., Singer, S. C., and Hunt, D. F. (1986) *J. Biol. Chem. 261*, 16363−16371.
35. Ferone, R., Hanlon, M. H., Singer, S. C., and Hunt, D. F. (1986) *J. Biol. Chem. 261*, 16356−16362.
36. Boger, D. L., Haynes, N. E., Kitos, P. A., Warren, M. S., Ramcharan, J., Marolewski, A. E., and Benkovic, S. J. (1997) *Bioorg. Med. Chem. 5*, 1817−1830.
37. Boger, D. L., Haynes, N. E., Warren, M. S., Ramcharan, J., Marolewski, A. E., Kitos, P. A., and Benkovic, S. J. (1997) *Bioorg. Med. Chem. 5*, 1847−1852.
38. Jansen, G., Westerhof, G. R., Kathmann, I., Rademaker, B. C., Rijksen, G., and Schornagel, J. H. (1989) *Cancer Res. 49*, 2455−2459.
39. Otwinowski, Z., and Minor, W. (1997) *Methods Enzymol. 276*, 307−326.
40. Matthews, B. W. (1968) *J. Mol. Biol. 33*, 491−497.
41. Rossmann, M. G. (1972) *The Molecular Replacement Method*, Gordon & Breach, New York.
42. Collaborative Computational Project Number 4 (1994) *Acta Crystallogr. D50*, 760−763.
43. Marangos, P. J., Loftus, T., Wiesner, J., Lowe, T., Rossi, E., Browne, C. E., and Gruber, H. E. (1990) *Epilepsia 31*, 239−246.
44. Jones, T. A., Zou, J. Y., Cowan, S. W., and Kjeldgaard, M. (1991) *Acta Crystallogr. A47*, 110−119.
45. Winn, M. D., Isupov, M. N., and Murshudov, G. N. (2001) *Acta Crystallogr. D57*, 122−133.
46. Laskowski, R. A., MacArthur, M. W., Moss, D. S., and Thornton, J. M. (1993) *J. Appl. Crystallogr. 26*, 283−291.
47. Esnouf, R. M. (1997) *J. Mol. Graphics Modell. 15*, 132−134.
48. Merritt, E. A., and Murphy, M. E. P. (1994) *Acta Crystallogr. D50*, 869−873.
49. Coon, S. I., Sanner, M. F., and Olson, A., J. (2001) *Ninth Annual International Python Conference*, Long Beach, CA.
50. Berman, H. M., Westbrook, J., Feng, Z., Gilliland, G., Bhat, T. N., Weissig, H., Shindyalov, I. N., and Bourne, P. E. (2000) *Nucleic Acids Res. 28*, 235−242.
51. Weiner, S. J., Kollman, P. A., Case, D. A., Singh, U. C., Ghio, C., Alagona, G., Profeta, S., and Weiner, P. (1984) *J. Am. Chem. Soc. 106*, 765−784.
52. Gasteiger, J., and Marsili, M. (1980) *Tetrahedron 36*, 3219−3228.
53. Goodsell, D. S., and Olson, A. J. (1990) *Proteins 8*, 195−202.
54. Morris, G. M., Goodsell, D. S., Halliday, R. S., Huey, R., Hart, W. E., Belew, R. K., and Olson, A. J. (1998) *J. Comput. Chem. 19*, 1639−1662.
55. Brodbeck, U., Schweikert, K., Gentinetta, R., and Rottenberg, M. (1979) *Biochim. Biophys. Acta 567*, 357−369.
56. Gelb, M. H., Svaren, J. P., and Abeles, R. H. (1985) *Biochemistry 24*, 1813−1817.
57. Arakawa, K., Inamasu, M., Matsumoto, M., Okumura, K., Yasuda, K., Akatsuka, H., Kawanami, S., Watanabe, A., Homma, K., Saiga, Y., Ozeki, M., and Iijima, I. (1997) *Chem. Pharm. Bull. 45*, 1984−1993.
58. Biovin, J., El Kaim, L., and Zard, S. Z. (1992) *Tetrahedron Lett. 33*, 1285−1288.
59. Biovin, J., El Kaim, L., and Zard, S. Z. (1995) *Tetrahedron 51*, 2573−2584.
60. Sanghani, S. P., and Moran, R. G. (1997) *Biochemistry 36*, 10506−10516.
61. Jansen, G., Kathmann, I., Rademaker, B. C., Braakhuis, B. J., Westerhof, G. R., Rijksen, G., and Schornagel, J. H. (1989) *Cancer Res. 49*, 1959−1963.
62. Caperelli, C. A., and Giroux, E. L. (1997) *Arch. Biochem. Biophys. 341*, 98−103.
63. Greasley, S. E., Marsilje, T. H., Yamashita, M. M., Cai, H., Benkovic, S. J., Boger, D. L., and Wilson, I. A. (2001) *Biochemistry 40*, 13538−13547.
64. Su, Y., Yamashita, M. M., Greasley, S. E., Mullen, C. A., Jennings, P. A., Warren, M. S., Benkovic, S. J., and Wilson, I. A. (1998) *J. Mol. Biol. 281*, 485−499.

BI034219C